Coherent control in ferromagnets driven by microwave radiation and spin polarized current

Marina Brik,* Nirel Bernstein, and Amir Capua†
Department of Applied Physics, The Hebrew University of Jerusalem, Jerusalem 91904, Israel

(Received 13 September 2020; revised 1 December 2020; accepted 2 December 2020; published 21 December 2020)

Coherent control is a method used to manipulate the state of matter using oscillatory electromagnetic radiation which interacts with the state in a nonequilibrium manner before the steady precessional state is reached. It is commonly applied in quantum processing applications. This technique is interesting in the context of ferromagnetic materials because of the ability to combine it with spintronics for the purpose of fundamental spin transport research, low-power information processing, and potentially future quantum bit (Qubit) applications. In this work we address the theoretical grounds of coherent manipulation in practical ferromagnetic systems. We study the electromagnetic radiation-driven interaction that is enhanced in the presence of spin-polarized current and map the conditions that allow coherent manipulation for which Rabi oscillations take place. The role of the magnetic anisotropy field is shown to act as an additional oscillatory driving field. We discuss the Gilbert losses in the context of effective coherence decay rates and show that it is possible to control these rates by application of a static spin current. The case of coherent manipulation using oscillatory spin current that is free of radiation is discussed as well. Our work paves the way towards spin current amplification as well as radiation-free coherent control schemes that may potentially lead to novel Qubits that are robust and scalable.

DOI: 10.1103/PhysRevB.102.224308

I. INTRODUCTION

Coherent control is a method of controlling dynamical processes using electromagnetic (EM) radiation that translates a dynamical system from one state to another. At its basis stands a nonadiabatic process which means that the system loses or gains energy during the interaction with the radiation. As opposed to the nonadiabatic process, the ferromagnetic resonance (FMR) experiment is an adiabatic process: A harmonic stimulus drives the system in steady state and the energy stored in the magnetic medium is constant over time. Similarly, the pump-probe type free-induction decay experiment in ferromagnets (FM) is also not considered a nonadiabatic interaction because the driving EM radiation is absent. However, the perturbed FMR interaction is a nonadiabatic process.

Studies of spin dynamics in magnetic media have been mainly carried out under either the adiabatic regime (e.g., Refs. [1–3]), or the free-induction decay regime (e.g., Refs. [4–7]). These regimes have played an increasingly important role in understanding spin transport processes in atomically engineered solid-state devices and key fundamental phenomena have been explored, e.g., spin angular momentum losses [8–10], the spin Hall effect (SHE) [11–15], the anomalous Hall effect [16], motion of magnetic domains [17–20], the spin transfer torques (STT) [21–23], and more.

The third dynamical regime of the nonadiabatic interaction has so far received little attention in the context of FM systems [24]. It can be considered as a hybrid dynamical regime which is a combination of the microwave-driven steady-state interaction [1–3] and the impulse stimulated free-induction decay [4–7] so that the EM radiation and the magnetization state are not in equilibrium and excessive energy is transferred back and forth between the two before the steady precessional state is reached. When the energy is exchanged periodically, Rabi oscillations arise that are characterized by the Rabi frequency and are the basis for coherent control similarly to a two-level system [25]. The analogy to quantum two-level system stems from the fact that the observables of angular momentum in two-level systems obey the classical equations of motion. In fact, Rabi's original theory [24] which was derived for a nuclear two-level spin system that is driven by an oscillatory field under the nonadiabatic interaction can be equally applied to an isolated electron or equivalently to a FM in the absence of the Gilbert losses and anisotropies under the macrospin limit. Furthermore, similarly to the two-level system, in the nonadiabatic interaction coherence plays a role in the sense that the outcome of the interaction is dependent on the initial phase relations between the magnetization state and the oscillatory torque [26]. Hence, a great deal of insight into the quantum world is gained from studies of the spin ensembles.

Because of the large gyromagnetic ratio of the electron, exploration of the nonadiabatic regime in FM systems often requires fast electronics and/or synchronization circuitry capable of operating in the GHz range. Hence, experimental studies of the nonadiabatic regime in magnetic solid-state systems is usually more cumbersome. In the work by Karenowska (Ref. [27]), a spatial nonequilibrium energy exchange was demonstrated between counterpropagating spin waves in yttrium iron garnets using artificial magnonic crystals. In these experiments a periodic spatial modulation fulfilled the role of the oscillatory signal whereas the effect was recognized to be valuable for signal processing purposes.

*marina.brik@mail.huji.ac.il
†amir.capua@mail.huji.ac.il

At the quantum limit, coherent control of single artificial magnetic spins was demonstrated using a scanning tunneling microscope [28]. In Ref. [28] magnetic Ti atoms were excited using microwaves to induce Rabi oscillations while initialization of the atoms was achieved by passing a DC spin current through the atom. This study was carried out in the time domain and the magnetization state was read out magnetoresistively.

Recently, we have demonstrated a hybrid time-frequency domain method to excite the nonadiabatic regime in magnetic media which we can describe as the pump-probe optically sensed ferromagnetic resonance [29]. In this method, Rabi oscillations were excited in a few Å-thick film of a CoFeB ferromagnet and in the presence of rf radiation following a perturbation by an intense ultrashort demagnetizing optical pulse. These experiments revealed a frequency chirp which was controllable by the static magnetic field and that the microwave field induced coherence in the inhomogeneously (IH)-broadened spin ensemble. Moreover, the experiments showed that according to Gilbert's damping theory the intrinsic relaxation times were tunable by proper choice of the external magnetic field and when taken long enough they eventually initiated a resonant spin mode locking of the system.

In the present work we provide the theoretical grounds for the nonadiabatic regime in a FM. We consider a system being driven into precession by microwave EM radiation and spin current. We compute the equations of motion for small deviations away from the steady precessional state. The deviations nutate at the Rabi frequency with a decaying amplitude. The frequency and decay rates of these nutations in a variety of circumstances are derived. To that end we combine the formalism of the adiabatic interaction in FMs and approaches that are commonly used to describe two-state quantum systems. We compare between the representation of the spin-lattice and transverse spin-polarization decay times, T_1 and T_2^*, used to describe quantum coherent phenomena and the Gilbert damping constant and IH broadening arising from Gilbert's damping theory. The influence of the injection of DC spin current on the effective coherence and decay times and the role of the magnetic anisotropy is studied. In addition, we present the case of using the AC spin current to drive the nonadiabatic dynamics instead of EM microwaves. We discuss the limitations of using AC STT as a driving force, and clarify its distinct nature compared to the ordinary rf EM field case.

Our work is presented as follows: We start by introducing the general conditions for observing Rabi oscillations in a magnetic system that is driven by a rf EM field. Next, we include the anisotropy fields and examine the case of the film having a perpendicular magnetic anisotropy (PMA) which is relevant for practical applications. We then add to our model a DC SHE. Specifically, we look into the influence of the injection of spin current on the overdamped interaction for which the magnetization simply decays and Rabi oscillations are not observable. Finally, the nonadiabatic interaction is studied in the presence of a driving oscillatory STT generated by the SHE.

II. MODEL AND RESULTS

A. Model framework: Rabi oscillations in FMs

Our analysis is carried out under the framework of the macrospin approximation. To that end we start with the Landau-Lifshitz-Gilbert (LLG) equation for the magnetization, $\vec{M}'$, in the presence of the effective field, $\vec{H}'_{\rm eff}$. Throughout the paper we use a prime to indicate variables in the lab frame of reference and the unprimed variables refer to the rotating system of coordinates. In the lab frame of reference

$$\frac{d\vec{M}'}{dt} = -\gamma(\vec{M}' \times \vec{H}'_{\rm eff}) + \frac{\alpha}{M_s}\left(\vec{M}' \times \frac{d\vec{M}'}{dt}\right), \tag{1}$$

in which M_s is the magnetization saturation, α is the Gilbert damping parameter, and γ is the gyromagnetic ratio. In spherical coordinates the LLG equation converts to

$$\begin{aligned} \dot{\theta}' &= \gamma H'_\varphi \\ \sin\theta'\dot{\varphi}' &= -\gamma H'_\theta, \end{aligned} \tag{2}$$

where H'_θ and H'_φ are the polar and azimuthal components of the effective field, respectively.

In order to study the nonadiabatic interaction, we convert Eq. (2) to a coordinate system rotating about the $\hat{z}'$ axis at the driving angular frequency, ω. In spherical coordinates, this corresponds to the substitutions $\theta' = \theta$ and $\varphi' = \varphi + \omega t$. Following linearization, we express the solution of Eq. (2) in the rotating frame by $\theta(t) = \theta_0 + \Delta\theta(t)$ and $\varphi(t) = \varphi_0 + \Delta\varphi(t)$ with $[\Delta\theta(t), \Delta\varphi(t)]$ being small deviations from equilibrium $(\theta_0, \ \varphi_0)$. $(\theta_0, \ \varphi_0)$ indicate the coordinates that the magnetization decays towards in the rotating frame and not the energy minimum in the lab frame as in conventional FMR models. Alternatively, in the lab frame, these coordinates correspond to the coordinates of the steady precessional state (up to a constant phase difference). $\Delta\theta(t)$ and $\Delta\varphi(t)$ are then expressed by their phasors $\Delta\theta = \Delta\theta_i \exp(-i\Omega t)$ and $\Delta\varphi = \Delta\varphi_i \exp(-i\Omega t)$, with $\Delta\theta_i$ and $\Delta\varphi_i$ being constants of the problem that are determined by the initial conditions. The complex frequency, Ω, consists of the real part responsible for the oscillatory component known as the generalized Rabi frequency, Ω_R^G, and of the imaginary part responsible for the dampening of the response, indicated by the decay rate, Γ, according to $\Omega = -i\Gamma + \Omega_R^G$. Rabi oscillations are generally observable when the decay time is longer than the Rabi cycle, namely, when $\Gamma < \Omega_R^G$ and the response becomes underdamped. When $\Gamma > \Omega_R^G$ the response becomes overdamped and the magnetic moment in the rotating frame decays exponentially towards $(\theta_0, \ \varphi_0)$ without oscillating. Finally, Ω_R^G is given by $\Omega_R^G = \sqrt{\Omega_\sigma^2 - \Gamma^2}$, where Ω_σ and Γ are obtained by satisfying the secular equation $\Omega^2 + i2\Omega\Gamma - \Omega_\sigma^2 = 0$ in the usual manner.

B. Fundamental interaction: EM-driven dynamics

1. Rabi frequency and linewidth

We first examine the microwave magnetic field-driven interaction that will also serve as a reference case. The external magnetic field of magnitude H_0 is chosen in the $\hat{z}'$ direction

while the oscillatory driving field of amplitude $h_{\rm rf}$ is applied along the $\hat{x}'$ axis. In the rotating frame under the rotating wave approximation, Eq. (2) becomes

$$\begin{aligned}\dot{\theta} &= -\frac{1}{2}\gamma h_{\rm rf}\sin\varphi - \alpha\sin\theta(\dot{\varphi}+\omega)\\ \sin\theta\dot{\varphi} &= \gamma\left(H_0 - \frac{\omega}{\gamma}\right)\sin\theta\\ &\quad -\frac{1}{2}\gamma h_{\rm rf}\cos\theta\cos\varphi + \alpha\dot{\theta}.\end{aligned} \tag{3}$$

$(\theta_0,\ \varphi_0)$ can be inferred from the equilibrium conditions $\dot{\theta} = \dot{\varphi} = 0$, while the time-dependent part of Eq. (3) gives

$$\begin{aligned}\Delta\dot{\theta} &= -\frac{1}{2}\gamma h_{\rm rf}\cos\varphi_0\Delta\varphi\\ &\quad -\alpha\sin\theta_0\Delta\dot{\varphi} - \alpha\omega\cos\theta_0\Delta\theta\\ \sin\theta_0\Delta\dot{\varphi} &= \gamma\left(H_0 - \frac{\omega}{\gamma}\right)\cos\theta_0\Delta\theta\\ &\quad +\frac{1}{2}\gamma h_{\rm rf}\cos\theta_0\sin\varphi_0\Delta\varphi\\ &\quad +\frac{1}{2}\gamma h_{\rm rf}\sin\theta_0\cos\varphi_0\Delta\theta + \alpha\Delta\dot{\theta}.\end{aligned} \tag{4}$$

The set of Eq. (4) describes the conventional problem of a two-level system [30] with the difference that the spin angular momentum losses are incorporated through Gilbert's damping theory [31]. The Gilbert damping in the LLG equation has a rigorous physical origin. It originates from a Rayleigh friction process that is included to model losses such as those mediated by the spin-orbit and exchange interactions. Hence, the energy dissipation rate in our model is inherently dependent on numerous parameters of the problem with the most critical of them being the frequency of the precessional motion and consequently the external magnetic field [29]. In contrast, in the Bloch-Bloembergen formalism the losses are incorporated through T_1 and T_2^* and are generally independent of the effective field of the problem. The IH broadening that arises from variations in local anisotropy fields can be added in our model by taking variations in the effective bias field to the first order [32]. Figure 1 highlights the differences between the two models.

To calculate the Rabi flopping frequency, Ω_σ and Γ can be determined from Eq. (5):

$$\begin{aligned}\Omega_\sigma &= \gamma\left\{\frac{1}{(\alpha^2+1)}\left(\left(\frac{\alpha\omega}{\gamma}\right)^2\cos^2\theta_0\right.\right.\\ &\quad \left.\left.+\left(H_0-\frac{\omega}{\gamma}\right)^2+\left(\frac{1}{2}h_{\rm rf}\right)^2\cos^2\varphi_0\right)\right\}^{1/2},\\ \Gamma &= \gamma\frac{\alpha}{2(\alpha^2+1)}\left(\frac{2\omega}{\gamma}\cos\theta_0+\left(H_0-\frac{\omega}{\gamma}\right)\cos\theta_0\right.\\ &\quad \left.+\frac{1}{2}h_{\rm rf}\sin\theta_0\cos\varphi_0+\frac{1}{2}h_{\rm rf}\frac{\cos\varphi_0}{\sin\theta_0}\right).\end{aligned} \tag{5}$$

On resonance $(H_0 - \frac{\omega}{\gamma}) = 0$ and the solutions for $(\theta_0,\ \varphi_0)$ require $\theta_0 = +90^\circ$ or $\varphi_0 = -90^\circ$. The solution $\theta_0 = +90$ and $\varphi_0 = -90^\circ$ corresponds to $\alpha\omega = \frac{1}{2}\gamma h_{\rm rf}$, which indicates the transition from the overdamped to underdamped dynamics.

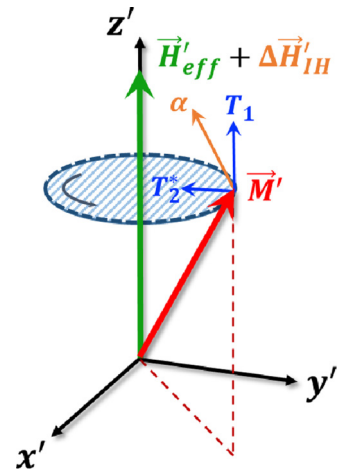

FIG. 1. Geometrical representation of the damping and relaxation torques and the IH broadening of Bloch-Bloembergen and Gilbert pictures. Blue arrows represent the lattice and transverse relaxation torques, T_1 and T_2^*, respectively. $\vec{H}'_{\rm eff}$ is the effective magnetic field. The Gilbert damping torque is indicated by the orange arrow and the IH broadening, $\Delta\vec{H}'_{IH}$, is modeled as variations in $\vec{H}'_{\rm eff}$.

In the underdamped regime in which Rabi oscillations are observable, $\alpha\omega < \frac{1}{2}\gamma h_{\rm rf}$, $\theta_0 = 90^\circ$, and $\varphi_0 = -\arcsin(2\alpha\omega/\gamma h_{\rm rf})$, resulting in

$$\begin{aligned}\Omega_R^G &= \gamma\sqrt{\left(\frac{1}{2}h_{\rm rf}\right)^2\cos^2(\varphi_0)\left(\frac{1}{(\alpha^2+1)}-\frac{\alpha^2}{(\alpha^2+1)^2}\right)},\\ \Gamma &= \frac{\alpha}{2(\alpha^2+1)}\gamma h_{\rm rf}\cos(\varphi_0),\end{aligned} \tag{6}$$

and when $\alpha\omega > \frac{1}{2}\gamma h_{\rm rf}$, $\varphi_0 = -90^\circ$ and $\theta_0 = \arcsin(\gamma h_{\rm rf}/2\alpha\omega)$ and the response is overdamped with

$$\begin{aligned}\Omega_R^G &= \gamma\sqrt{\left(\frac{\alpha\omega}{\gamma}\right)^2\cos^2(\theta_0)\left(\frac{1}{(\alpha^2+1)}-\frac{1}{(\alpha^2+1)^2}\right)},\\ \Gamma &= \frac{\alpha\omega}{(\alpha^2+1)}\cos(\theta_0),\end{aligned} \tag{7}$$

The calculated results are presented in Fig. 2. The given geometry is shown in Fig. 2(a). Figure 2(b) illustrates Ω_R^G and Γ for $\alpha = 0.01$ and 10 GHz on resonance as a function of the normalized field $\frac{\gamma h_{\rm rf}}{2\alpha\omega}$. The data resemble closely the dependence of the resonance frequency of a FM on the applied field when the external magnetic field is applied perpendicularly to the easy axis. In this case the quantity $\frac{1}{2}h_{\rm rf}$ fulfills the same role as the static external field, $\frac{\alpha\omega}{\gamma}$ plays the role of the effective anisotropy field, and the easy axis is the rotation axis, $\hat{z}'$. This effective anisotropy field arises from the projection of the Gilbert damping torque into the rotating frame and is hence dependent on both α and ω, and similarly to an actual anisotropy field the torque that arises from it depends on the angle between the magnetization and the easy axis. For $\alpha\omega > \frac{1}{2}\gamma h_{\rm rf}$, Γ rapidly increases with decreasing $h_{\rm rf}$ and becomes more than two orders of magnitude greater than Ω_R^G as shown in the inset so that Rabi oscillations are not obtained. When $\alpha\omega < \frac{1}{2}\gamma h_{\rm rf}$ this behavior abruptly changes and Ω_R^G becomes much greater than Γ with increasing $h_{\rm rf}$ giving rise

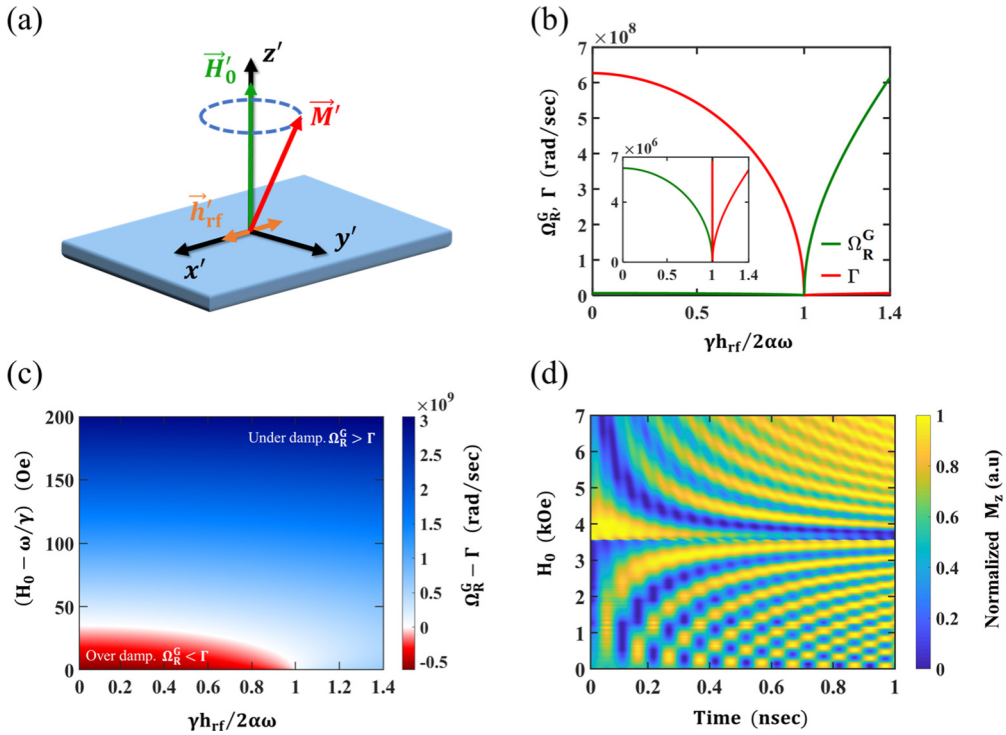

FIG. 2. (a) Geometry of the rf EM-driven dynamics. (b) Ω_R^G, Γ for zero detuning. Inset shows closeup of Ω_R^G at $\gamma h_{rf}/2\alpha\omega < 1$. (c) $\Omega_R^G - \Gamma$ as a function of the detuning. The red zone indicates the overdamped region, while the blue zone is the underdamped region. (d) Normalized and shifted temporal responses as a function of H_0 calculated numerically for $h_{rf} = 20$ Oe. The slight high-frequency modulation observed as a background arises from the counter-rotating terms that are neglected in the model. Results are presented for $\alpha = 0.01$ and 10 GHz.

to Rabi nutations. Figure 2(c) illustrates the difference $\Omega_R^G - \Gamma$ as a function of the detuning, $(H_0 - \frac{\omega}{\gamma})$, and the normalized field from which the oscillatory nature can be determined. Starting from $(H_0 - \frac{\omega}{\gamma}) = \sim 30$ Oe the behavior is always oscillatory irrespective of h_{rf}. Figure 2(d) shows a typical temporal response for various H_0 values for which the response is overdamped at resonance and away from resonance becomes oscillatory.

2. *Interpretation of the Gilbert damping torque in the rotating frame*

In the rotating frame of reference, the damping torque can be interpreted in a comprehensive manner providing further insight to the nonadiabatic interaction. In Cartesian coordinates Eq. (1) transforms to

$$\frac{d\vec{M}}{dt} = -\gamma\vec{M} \times \left(\left(\vec{H}_0 - \frac{\vec{\omega}}{\gamma}\right) + \vec{h}_{rf}\right) + \frac{\alpha}{M_s}\left(\vec{M} \times \frac{\delta\vec{M}}{\delta t}\right) - \frac{\alpha}{M_s}\vec{M} \times (\vec{M} \times \vec{\omega}), \quad (8)$$

where $\vec{\omega}$ is the vector $(0, 0, \omega)$ and $\vec{h}_{rf}$ is the rf field. The first term on the right-hand side of Eq. (8) is the effective field $(\vec{H}_0 - \frac{\vec{\omega}}{\gamma}) + \vec{h}_{rf}$ which $\vec{M}$ primarily precesses about. The second term on the right-hand side of Eq. (8) is identical to the Gilbert damping term in the LLG equation and is responsible for the decay of the magnetic field towards the effective field. The third term, $-\frac{\alpha}{M_s}\vec{M} \times (\vec{M} \times \vec{\omega})$, does not appear in the LLG equation in the lab frame. It behaves as a nonconserving torque that has the form of the antidamping STT term of the Landau-Lifshitz-Gilbert-Slonczewski (LLGS) equation. This term gives rise to the effective field $\frac{\alpha}{M_s}(\vec{M} \times \frac{\vec{\omega}}{\gamma})$ and scales with $\alpha\omega$. In steady state, $\frac{\delta\vec{M}}{\delta t} = 0$, it balances the primary field $(\vec{H}_0 - \frac{\vec{\omega}}{\gamma}) + \vec{h}_{rf}$ and causes the system to decay towards a new steady state different than the one dictated solely by the primary field. Hence, this torque can be used as an additional control in a coherent manipulation scheme. Before steady state is reached its contribution to Ω_σ and hence also to Ω_R^G is readily seen in Eq. (5) where it appears as an additional term in the Euclidean norm of the fields consisting of $\vec{h}_{rf}$, $(\vec{H}_0 - \frac{\vec{\omega}}{\gamma})$, and $\alpha\vec{\omega}/\gamma$ that eventually determine the Rabi frequency. This STT-like torque can be enhanced by increasing the driving frequency which is analogous to increasing the spin current in the LLGS equation.

3. *Large-angle nonadiabatic interaction*

The analytical model addresses small deviations from steady precessional state. For large deviations, the nonadiabatic response becomes nonlinear, giving rise to the generation of higher harmonics. We examine this nonlinearity numerically [33–35]. A typical representative temporal response in the lab frame of reference is presented in Fig. 3 at 10 GHz and h_{rf} of 90 Oe on resonance (following the experiments of Ref. [29]). In this example the magnetization was initialized to the $\hat{z}'$ direction and traversed the full swing towards the

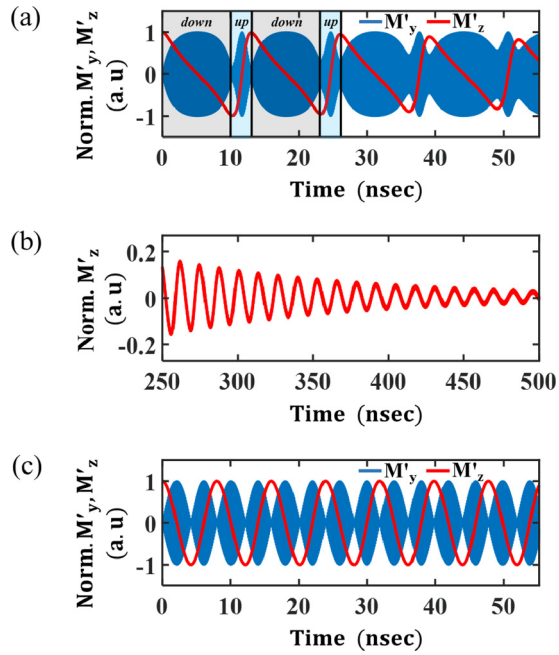

FIG. 3. Large signal response calculated numerically. (a) Response calculated at 10 GHz and $\alpha = 0.01$. (b) Same simulation presented in (a) at later times. (c) Same conditions as in (a) but with $\alpha = 0.001$.

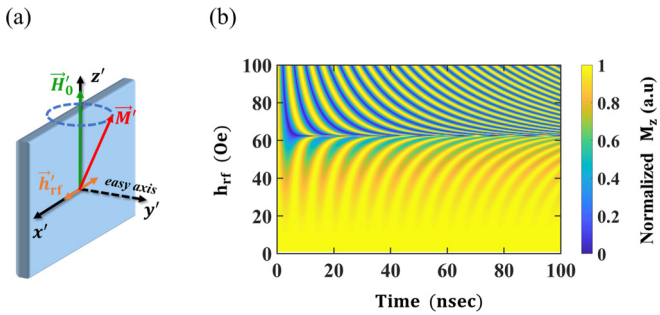

FIG. 4. (a) Geometry of the rf EM-driven dynamics in a PMA sample. (b) Temporal M_z responses as a function of $h_{\rm rf}$ calculated numerically for $H_0 = \frac{\omega}{\gamma}$ (quasiresonance), effective anisotropy field of 120 Oe, and $\alpha = 10^{-4}$.

$-\hat{z}'$ direction. Figure 3(a) shows the response for α of 0.01. The figure depicts M'_z which is proportional to the energy of the system and M'_y. A nonlinear response consisting of higher harmonics is readily seen as well as an asymmetric behavior as M'_z evolves, namely, as energy is absorbed or emitted. The "down" transition is slower than the "up" transition for which $\vec{M}'$ aligns with $\vec{H}'_0$. This is also readily seen on the M'_y component which stretches or compresses in time depending on the up or down transition. At later times, as the response further decays and $\vec{M}'$ precesses at small angles near the steady state, the asymmetry vanishes and a harmonic response is revealed [Fig. 3(b)]. This behavior is highly dependent on the Gilbert damping as shown in Fig. 3(c). When α is reduced to a value of 0.001 the nonlinearity vanishes and M'_z oscillates at a single frequency according to the analytical model. The effect of the Gilbert damping on the nonlinear nature of the response is understood by examining the acting torques. The torque arising from the applied magnetic fields, namely rf and DC fields, $\frac{d\vec{M}'}{dt_{\rm app.}}$, can be decomposed into two components: a tangential component, $\frac{d\vec{M}'}{dt_{\parallel}}$, responsible for the primary longitudinal precessional motion, and a transverse component, $\frac{d\vec{M}'}{dt_{\perp}}$, responsible for the "downward"/"upward" transition of $\vec{M}'$. When $\vec{M}'$ shifts towards $-\hat{z}'$, the transverse component, $\frac{d\vec{M}'}{dt_{\perp}}$, is balanced by the Gilbert damping torque and the transition occurs at a slower rate. Likewise, when $\vec{M}'$ shifts towards $\hat{z}'$ the transverse component, $\frac{d\vec{M}'}{dt_{\perp}}$, is enhanced by the Gilbert damping torque. Therefore, the Gilbert torque is responsible for the asymmetry in the upward/downward transition rates. Finally, as $\vec{M}'$ further decays towards steady precessional state the applied torque is primarily tangential and the transverse torque component $\frac{d\vec{M}'}{dt_{\perp}}$ is negligible, resulting in a harmonic response. This behavior is more prominent the greater α is [Figs. 3(a) and 3(c)]. Hence, changes in α can be readily seen on the nonlinear nonadiabatic response, thereby providing an additional way to investigate the loss mechanisms.

4. Inclusion of magnetic anisotropy

Practical magnetic systems exhibit magnetic anisotropy fields such as demagnetization and/or crystalline anisotropies. We focus on the case of a sample having PMA such as the geometry studied in Ref. [29] which is usually more important for technological purposes and allows high density and lower crosstalk between devices in practical applications.

The modeled geometry is illustrated in Fig. 4(a). The easy axis of magnetization is set along $\hat{y}'$. The effective anisotropy is $H_{K\rm eff} = \frac{2K_u}{M_s} - 4\pi M_s$, where K_u is the crystalline anisotropy constant. The analysis was carried out under the condition $H_0 > H_{K\rm eff}$ for which the precession takes place around the $\hat{z}'$ axis in the lab frame. Under these conditions the problem has a closed form analytical solution. Hence, Eq. (4) becomes

$$\begin{aligned}
\Delta\dot{\theta} &= -\frac{1}{2}\gamma h_{\rm rf}\cos\varphi_0\Delta\varphi - \alpha\sin\theta_0\Delta\dot{\varphi} - \alpha\omega\cos\theta_0\Delta\theta \\
\sin\theta_0\Delta\dot{\varphi} &= -\frac{\gamma H_{K\rm eff}}{2}\cos 2\theta_0\Delta\theta + \gamma\left(H_0 - \frac{\omega}{\gamma}\right)\cos\theta_0\Delta\theta \\
&\quad + \frac{1}{2}\gamma h_{\rm rf}\cos\theta_0\sin\varphi_0\Delta\varphi \\
&\quad + \frac{1}{2}\gamma h_{\rm rf}\sin\theta_0\cos\varphi_0\Delta\theta + \alpha\Delta\dot{\theta} \qquad (9)
\end{aligned}$$

while $(\theta_0,\ \varphi_0)$ is found as before.

The solutions for Ω_σ and Γ are

$$\Omega_\sigma = \gamma\left\{\frac{1}{(\alpha^2+1)}\left(\left(\frac{\alpha\omega}{\gamma}\right)^2\cos^2\theta_0 - \frac{1}{2}h_{\rm rf}\frac{1}{2}H_{K\rm eff}\frac{\cos 2\theta_0\cos\varphi_0}{\sin\theta_0} + \frac{1}{2}h_{\rm rf}\left(H_0-\frac{\omega}{\gamma}\right)\frac{\cos\theta_0\cos\varphi_0}{\sin\theta_0} + \left(\frac{1}{2}h_{\rm rf}\right)^2\cos^2\varphi_0\right)\right\}^{1/2},$$
$$\Gamma = \gamma\frac{\alpha}{2(\alpha^2+1)}\left(\frac{2\omega}{\gamma}\cos\theta_0 - \frac{H_{K\rm eff}}{2}\cos 2\theta_0 + \left(H_0-\frac{\omega}{\gamma}\right)\cos\theta_0 + \frac{1}{2}h_{\rm rf}\sin\theta_0\cos\varphi_0 + \frac{1}{2}h_{\rm rf}\frac{\cos\varphi_0}{\sin\theta_0}\right). \quad (10)$$

For small α, small $h_{\rm rf}$, and quasiresonance conditions $(H_0 - \frac{\omega}{\gamma}) = 0$, $\varphi_0 = -180^\circ$ and the condition for θ_0 is $\sin\theta_0 = h_{\rm rf}/H_{K\rm eff}$. Substituting the above conditions into the Ω_σ term in Eq. (10), we get

$$\Omega_R^G = \gamma\sqrt{\left(\frac{H_{K\rm eff}}{2}\right)^2 - \left(\frac{h_{\rm rf}}{2}\right)^2}. \quad (11)$$

Equation (11) has the familiar form of resonance frequency for the PMA case where the external field is applied perpendicular to the easy axis. Thus, in the rotating frame $h_{\rm rf}$ takes the role of DC field applied perpendicularly to the easy axis. In comparison with the PMA case [36], $\frac{1}{2}H_{K\rm eff}$ appears as an effective anisotropy field in the rotating frame. The dependence of Ω_R^G on $h_{\rm rf}$ in Eq. (11) is fundamentally different from its general dependence in standard two-level systems. Here Ω_R^G decreases with increasing $h_{\rm rf}$ whereas in conventional two-level systems Ω_R^G increases with the driving-field amplitude. In conventional two-level systems the driving-field amplitude determines the rate at which the occupation probabilities evolve, therefore Ω_R^G generally increases with $h_{\rm rf}$. In contrast, in Eq. (11) Ω_R^G decreases with $h_{\rm rf}$ and is due to the role played by the anisotropy field which effectively acts as an additional oscillatory driving field. Therefore, the observed response deviates from the conventional two-level system behavior until $h_{\rm rf}$ reaches the limit of $\frac{1}{2}H_{K\rm eff}$. The numerical model shows this behavior as well. The temporal responses presented in Fig. 4(b) show that Ω_R^G decreases as $h_{\rm rf}$ increases up to 60 Oe ($\frac{1}{2}H_{K\rm eff}$). Above 60 Oe $h_{\rm rf}$ overcomes the anisotropy field and Ω_R^G increases with $h_{\rm rf}$ as expected.

C. Interaction in the presence of DC spin current

From a technological point of view, a static STT may play an important role in the nonadiabatic interaction in magnetic systems because it can be used to actively tune the decay rates according to the LLGS equation [22,23]. Specifically, STT can be used to extend the coherence time of the system making the FM system a versatile platform for coherent control schemes. In the model derived hereon we consider the antidamping-like STT and assume that the spin current is generated by the SHE in a heavy metal-FM bilayer [37]. Hence, a DC charge current of magnitude $J_c^{\rm DC}$ is applied along the $\hat{x}'$ direction and generates a spin current density $J_s\hat{y}'$ with spin angular momentum aligning in the $\hat{z}'$ direction. Figure 5 illustrates the modeled geometry. The presence of spin current introduces the torque $\frac{\gamma H_{\rm SHE,\ DC}}{M_s}(\vec{M}'\times(\vec{M}'\times\hat{s}'))$ into Eq. (1). Here $\hat{s}'$ is a unit vector in the direction of the injected spin angular momentum and $H_{\rm SHE,\ DC}$ is the SHE parameter defined by $H_{\rm SHE,\ DC} = \frac{\hbar\theta_{\rm SH}J_c^{\rm DC}}{2eM_s t_{\rm FM}}$ where $\hbar$ is the reduced Planck constant, e is the electron charge, $\theta_{\rm SH}$ is the spin Hall angle (SHA), and $t_{\rm FM}$ is the thickness of the FM layer into which the spin current is injected. With these substitutions Eq. (4) becomes

$$\Delta\dot{\theta} = -\frac{1}{2}\gamma h_{\rm rf}\cos\varphi_0\Delta\varphi - \alpha\sin\theta_0\Delta\dot{\varphi} - (\alpha\omega - \gamma H_{\rm SHE,\ DC})\cos\theta_0\Delta\theta$$
$$\sin\theta_0\Delta\dot{\varphi} = \gamma\left(H_0-\frac{\omega}{\gamma}\right)\cos\theta_0\Delta\theta + \frac{1}{2}\gamma h_{\rm rf}\cos\theta_0\sin\varphi_0\Delta\varphi + \frac{1}{2}\gamma h_{\rm rf}\sin\theta_0\cos\varphi_0\Delta\theta + \alpha\Delta\dot{\theta}, \quad (12)$$

resulting in Ω_σ and $\Delta\Omega$:

$$\Omega_\sigma = \gamma\left\{\frac{1}{(\alpha^2+1)}\left(\left(H_{\rm SHE,\ DC} - \frac{\alpha\omega}{\gamma}\right)^2\cos^2\theta_0 + \left(H_0-\frac{\omega}{\gamma}\right)^2 + \left(\frac{1}{2}h_{\rm rf}\right)^2\cos^2\varphi_0\right)\right\}^{1/2}$$
$$\Gamma = \gamma\frac{1}{2(\alpha^2+1)}\left(2\left(\frac{\alpha\omega}{\gamma} - H_{\rm SHE,\ DC}\right)\cos\theta_0 + \alpha\left(H_0-\frac{\omega}{\gamma}\right)\cos\theta_0 + \alpha\frac{1}{2}h_{\rm rf}\sin\theta_0\cos\varphi_0 + \alpha\frac{1}{2}h_{\rm rf}\frac{\cos\varphi_0}{\sin\theta_0}\right). \quad (13)$$

Equation (13) shows that the spin current compensates the Gilbert damping term according to the difference $\frac{\alpha\omega}{\gamma} - H_{\rm SHE,\ DC}$. Equation (13) reveals that for the critical case of $H_{\rm SHE,\ DC} = \frac{\alpha\omega}{\gamma}$ which may be achieved in realistic systems having SHA of 0.15, e.g., Pt, W [12,13] the response is always underdamped, namely, $\Gamma < \Omega_R^G$, and Rabi oscillations appear irrespective of the magnitude of $h_{\rm rf}$. Obviously, these oscillations still decay as $\Gamma \neq 0$. To examine the influence of the injected spin current on the existence of Rabi oscillations and the damping rate we explored the interaction under resonance conditions. Figure 6 illustrates the temporal responses from which the transition between the overdamped and underdamped regimes for various charge current levels is seen. The figure shows M_z as a function of $h_{\rm rf}$ with $\alpha = 0.01$,

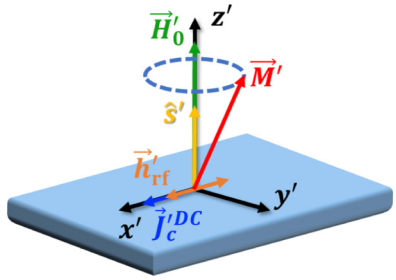

FIG. 5. Geometry of the EM rf-driven dynamics in the presence of DC spin current indicated by $\vec{J}_c'^{\rm DC}$ in the lab frame.

$M_s = 300\,\mathrm{emu/cm^3}$, $\theta_{\rm SH} = 0.15$, and $t_{\rm FM} = 11.5$ Å corresponding to Ref. [37]. Figure 6(a) presents the case with no spin current. It is seen that the transition between the overdamped and underdamped responses occurs at $h_{\rm rf} = 71$ Oe above which Rabi oscillations take place. When the DC current is increased the threshold reduces up to the point of $H_{\rm SHE,\,DC} = \frac{\alpha\omega}{\gamma}$ [Fig. 6(c)] in which the oscillations are obtained for any value of $h_{\rm rf}$. As the DC current is further increased, the threshold in $h_{\rm rf}$ increases again [Figs. 6(d)–6(f)]. This behavior stems from the fact that when $\alpha < \frac{\gamma H_{\rm SHE,\,DC}}{\omega}$ the term $2\gamma(\frac{\alpha\omega}{\gamma} - H_{\rm SHE,\,DC})\cos\theta_0$ in Eq. (13) adds a positive contribution to the damping rate. Thus, at high DC currents the Rabi oscillations eventually become overdamped. Most importantly, Fig. 6 shows that when Rabi oscillations take place the coherence times can be tuned by the DC spin current. This is seen from the varying decay rates as marked by the guiding red dashed lines in Figs. 6(a)–6(c). It is seen that as $J_c^{\rm DC}$ increases to the critical value (2.5×10^6 A/cm^2 in our case) the coherence times extend.

D. AC STT-driven nonadiabatic dynamics

Inclusion of AC charge current creates an AC STT which serves as an alternative driving force. A driving force of this kind is advantageous over the rf-driven case for scalability purposes since it does not require a radiating microantenna but only physical contact to the device. However, the AC STT driving force has a different nature compared to the ordinary Zeeman oscillatory magnetic field. We include the AC STT by replacing $\vec{h}'_{\rm rf}$ in Eq. (1) with an AC charge current density $\vec{J}_c^{\rm AC} = J_0\cos(\omega t)\hat{y}'$. The AC charge current is converted by the SHE to an AC spin current density $J_s\hat{z}'$ having $\hat{s}'$ in the $\hat{x}'$ direction which introduce a STT term of $\frac{\gamma h_{\rm SHE,\,AC}}{M_s}(\vec{M}'\times(\vec{M}'\times\hat{s}'))$ in Eq. (1). $h_{\rm SHE,\,AC}$ is the SHE parameter as in Sec. II C, that refers now to an AC current. The geometry is presented in Fig. 7(a). The $\vec{J}_c^{\rm AC}$ direction was chosen such that $\hat{s}'$ is orthogonal to the static magnetization equilibrium vector in the lab frame $\vec{M}'_0$. Following linearization, the AC STT in the lab frame equals approximately $\frac{\gamma h_{\rm SHE,\,AC}}{M_s}(\vec{M}'_0\times(\vec{M}'_0\times\hat{s}'))$. Thus, if $\vec{M}'_0$ and $\hat{s}'$ are collinear, the AC STT vanishes. The time-dependent equations become

$$\Delta\dot{\theta} = \frac{1}{2}\gamma h_{\rm SHE,\,AC}\cos\theta_0\sin\varphi_0\Delta\varphi + \frac{1}{2}\gamma h_{\rm SHE,\,AC}\sin\theta_0\cos\varphi_0\Delta\theta - \alpha\sin\theta_0\Delta\dot{\varphi} - \alpha\omega\cos\theta_0\Delta\theta\,,$$
$$\sin\theta_0\Delta\dot{\varphi} = \gamma\left(H_0 - \frac{\omega}{\gamma}\right)\cos\theta_0\Delta\theta + \frac{1}{2}\gamma h_{\rm SHE,\,AC}\cos\varphi_0\Delta\varphi + \alpha\Delta\dot{\theta}, \tag{14}$$

and Ω_σ and Γ for this case are given by

$$\Omega_\sigma = \gamma\left\{\frac{1}{(\alpha^2+1)}\left(\left(\frac{\alpha\omega}{\gamma}\right)^2 + \left(H_0 - \frac{\omega}{\gamma}\right)^2\cos^2\theta_0 + \left(\frac{1}{2}h_{\rm SHE,\,AC}\right)^2\cos^2\varphi_0\right)\right\}^{1/2}$$
$$\Gamma = \gamma\frac{1}{2(\alpha^2+1)}\left(\frac{\alpha\omega}{\gamma}\cos\theta_0 + 2\alpha\left(H_0 - \frac{\omega}{\gamma}\right)\cos\theta_0 - \frac{1}{2}h_{\rm SHE,\,AC}\sin\theta_0\cos\varphi_0 - \frac{1}{2}h_{\rm SHE,\,AC}\frac{\cos\varphi_0}{\sin\theta_0}\right). \tag{15}$$

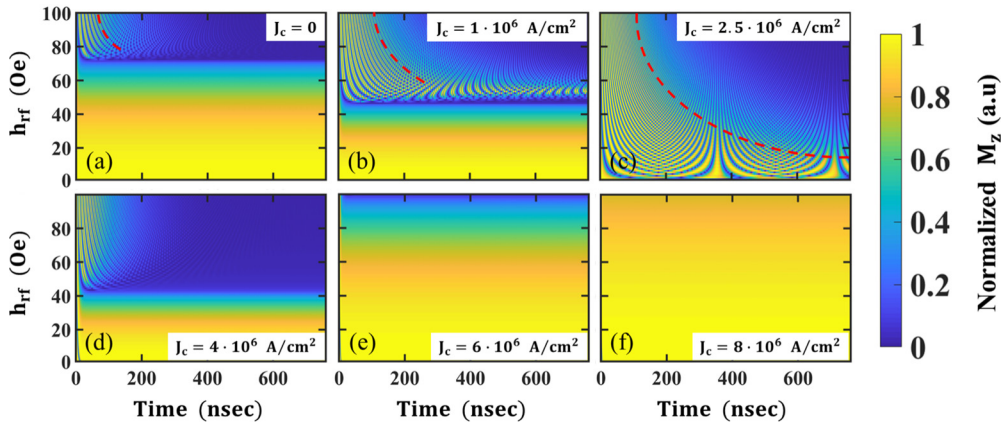

FIG. 6. Temporal responses as a function of $h_{\rm rf}$ calculated numerically for $J_c^{\rm DC}$ levels of 0 A/cm^2 to 8×10^6 A/cm^2 [(a) to (f)]. The red dashed guiding lines indicate the varying decay rates.

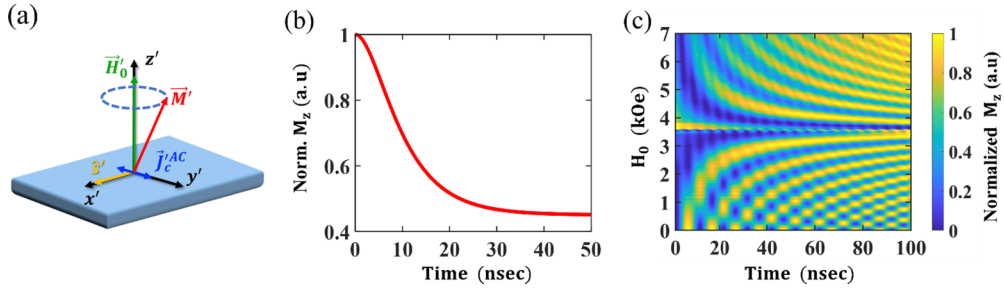

FIG. 7. FM system driven by AC STT. (a) Geometry of the AC STT driven nonadiabatic dynamics. (b) Response on resonance $(H_0 - \frac{\omega}{\gamma}) = 0$ for AC charge current density $\vec{J}_c^{\prime AC}$ with amplitude of $J_0 = 1 \times 10^6$ A/cm^2 and $\alpha = 0.001$. (c) Normalized and shifted temporal responses as a function of H_0 calculated numerically for the same J_0 value as in (b) and $\alpha = 0.005$.

To understand the general behavior of the solution we assume very small α and resonance conditions. From Eq. (15) it is seen that Γ takes a nonzero value even when $\alpha \to 0$; thus, the AC STT contributes to the decay term. From steady state we find $(\theta_0,\ \varphi_0) = (90^\circ, 180^\circ)$. Substituting $(\theta_0,\ \varphi_0)$ into Eq. (15) we get $\Omega_R^G = 0$. Hence, the response is overdamped [Fig. 7(b)] regardless of the $h_{\mathrm{SHE,\ AC}}$ value even in the absence of damping in contrast to the h_{rf}-driven case. It can be further verified that the overdamped response persists in the vicinity of resonance as long as $|(H_0 - \frac{\omega}{\gamma})| < \frac{1}{2}h_{\mathrm{SHE,\ AC}}$. This distinctly different behavior of the AC STT compared to the rf magnetic field case can be understood by observing Eq. (8) in the rotating frame in which $\vec{h}_{\mathrm{rf}}$ appears in the primary torque term $-\gamma\vec{M} \times ((\vec{H}_0 - \frac{\vec{\omega}}{\gamma}) + \vec{h}_{\mathrm{rf}})$. In contrast, when the system is driven solely by AC STT the primary torque vanishes on resonance, leaving only the AC dampinglike STT. For this reason, an additional DC STT cannot excite Rabi oscillations under resonance conditions, but only change the steady state. Away from resonance conditions and for $|(H_0 - \frac{\omega}{\gamma})| > \frac{1}{2}h_{\mathrm{SHE,\ AC}}$ Rabi oscillations are observable.

When losses are included in addition, a DC STT applied in the geometry of Sec. II C affects the losses in the same manner as in the $\vec{h}_{\mathrm{rf}}$ case where it extends the coherence time as long as $H_{\mathrm{SHE,\ DC}} \leqslant \frac{\alpha\omega}{\gamma}$. When $H_{\mathrm{SHE,\ DC}} > \frac{\alpha\omega}{\gamma}$, the coherence time decreases and for relatively high $H_{\mathrm{SHE,\ DC}}$ values the oscillations are totally suppressed. In the current analysis, the fieldlike term of the AC STT was neglected since in many material systems it is much smaller than the dampinglike term. However, when the fieldlike term is not negligible, it can excite Rabi oscillations even on resonance because its form is identical to the $\vec{h}_{\mathrm{rf}}$ torque and hence appears in the primary precessional torque term of Eq. (8). Figure 7(c) shows the temporal responses of M_z as a function of H_0. It is readily seen that despite the differences between the $\vec{h}_{\mathrm{rf}}$ and the AC STT cases especially on resonance, the AC STT-driven dynamics qualitatively behave in the same manner as the $\vec{h}_{\mathrm{rf}}$-driven interaction [Fig. 2(d)].

Finally, when the magnetic anisotropy is included, it can be verified that for the same geometry introduced earlier (Sec. II B 4), Eq. (15) takes the form

$$\begin{aligned}
\Omega_\sigma = \gamma\Bigg\{ & \frac{1}{(\alpha^2+1)}\Bigg(\left(\frac{\alpha\omega}{\gamma}\right)^2 - \frac{1}{2}h_{\mathrm{SHE,\ AC}}\left(H_0 - \frac{\omega}{\gamma}\right)\frac{\cos^2\theta_0 \sin\varphi_0}{\sin\theta_0} \\
& + \frac{1}{2}h_{\mathrm{SHE,\ AC}}\frac{1}{2}H_{k\mathrm{eff}}\frac{\cos 2\theta_0 \cos\theta_0 \sin\varphi_0}{\sin\theta_0} + \left(\frac{1}{2}h_{\mathrm{SHE,\ AC}}\right)^2\cos^2\varphi_0\Bigg)\Bigg\}^{1/2} \\
\Gamma = \gamma & \frac{1}{2(\alpha^2+1)}\Bigg(\frac{\alpha\omega}{\gamma}\cos\theta_0 + \alpha\left(H_0 - \frac{\omega}{\gamma}\right)\cos\theta_0 - \alpha\frac{1}{2}H_{k\mathrm{eff}}\cos 2\theta_0 \\
& - \alpha\frac{1}{2}h_{\mathrm{SHE,\ AC}}\frac{\cos\theta_0 \sin\varphi_0}{\sin\theta_0} - \frac{1}{2}h_{\mathrm{SHE,\ AC}}\sin\theta_0\cos\varphi_0 - \frac{1}{2}h_{\mathrm{SHE,\ AC}}\frac{\cos\varphi_0}{\sin\theta_0}\Bigg).
\end{aligned} \tag{16}$$

For $\alpha \to 0$ and resonance conditions the steady-state equations give $\varphi_0 = 90^\circ$ and the condition for θ_0 is $\sin 2\theta_0 = h_{\mathrm{SHE,\ AC}}/0.5H_{K\mathrm{eff}}$, for $h_{\mathrm{SHE,\ AC}} < H_{K\mathrm{eff}}$. Inserting these conditions into Eq. (16), we get $\Omega_R^G = \sqrt{\Omega_\sigma^2 - \Gamma^2} = \sqrt{\frac{1}{2}\gamma h_{\mathrm{SHE,\ AC}}\frac{1}{2}\gamma H_{k\mathrm{eff}}\frac{\cos 2\theta_0 \cos\theta_0}{\sin\theta_0}}$. Thus, when the anisotropy fields are included, $\Omega_R^G \neq 0$ and Rabi oscillations take place on resonance (quasiresonance).

III. SUMMARY

In this work we examined the nonadiabatic interaction which is the basis for coherent control schemes in magnetic materials and relied on a hybrid two-level/adiabatic interaction in FMs formalism. We explored the ordinary nonadiabatic interaction driven by rf field and mapped the conditions for reaching the Rabi oscillations for which coherent

control is made possible. We studied the energy transfer rates and showed that at large angles of precession and large α values the absorption and emission rates become highly nonsymmetric. Furthermore, this nonlinear nonadiabatic response provided an additional way to investigate the loss mechanisms. We demonstrated that it is possible to control the effective coherence time by the injection of DC current and explored the nonadiabatic interaction in a system driven by an alternative driving source, namely, the AC STT, and concluded that there are no Rabi oscillations on resonance, as long as the AC STT fieldlike term is negligible. However, it is possible to get on-resonance Rabi oscillations if the fieldlike term is non-negligible and this can motivate the search for magnetic materials that possess significant STT fieldlike term. Extensions of our work include complementing the existing experimental work to fully map the nonadiabatic regime in FM systems as well as to discuss a truly coherent control scheme that relays on the principles outlined here as well as coherent spin current amplification schemes (to be discussed in a follow-up paper). Further into the future, STT can be utilized as a versatile platform for coherent control schemes to be used in the manipulation of Qubits.

[1] S. S. Kalarickal, P. Krivosik, M. Wu, C. E. Patton, M. L. Schneider, P. Kabos, T. J. Silva, and J. P. Nibarger, Ferromagnetic resonance linewidth in metallic thin films: Comparison of measurement methods, J. Appl. Phys. **99**, 093909 (2006).

[2] J. M. Beaujour, D. Ravelosona, I. Tudosa, E. E. Fullerton, and A. D. Kent, Ferromagnetic resonance linewidth in ultrathin films with perpendicular magnetic anisotropy, Phys. Rev. B **80**, 180415(R) (2009).

[3] Y. Zhao, Q. Song, S.-H. Yang, T. Su, W. Yuan, S. Parkin, J. Shi, and W. Han, Experimental investigation of temperature-dependent Gilbert damping in permalloy thin films, Sci. Rep. **6**, 22890 (2016).

[4] E. Beaurepaire, J. C. Merle, A. Daunois, and J. Y. Bigot, Ultrafast Spin Dynamics in Ferromagnetic Nickel, Phys. Rev. Lett. **76**, 4250 (1996).

[5] T. J. Silva, C. S. Lee, T. M. Crawford, and C. T. Rogers, Inductive measurement of ultrafast magnetization dynamics in thin-film Permalloy, J. Appl. Phys. **85**, 7849 (1999).

[6] J.-Y. Bigot, M. Vomir, and E. Beaurepaire, Coherent ultrafast magnetism induced by femtosecond laser pulses, Nat. Phys. **5**, 515 (2009).

[7] J.-Y. Bigot, Ultrafast magnetism: Down to the nanometre scale, Nat. Mater. **12**, 283 (2013).

[8] G. Malinowski, K. C. Kuiper, R. Lavrijsen, H. J. M. Swagten, and B. Koopmans, Magnetization dynamics and Gilbert damping in ultrathin $Co_{48}Fe_{32}B_{20}$ films with out-of-plane anisotropy, Appl. Phys. Lett. **94**, 102501 (2009).

[9] M. A. W. Schoen, D. Thonig, M. L. Schneider, T. J. Silva, H. T. Nembach, O. Eriksson, O. Karis, and J. M. Shaw, Ultra-low magnetic damping of a metallic ferromagnet, Nat. Phys. **12**, 839 (2016).

[10] Y. Sun, H. Chang, M. Kabatek, Y.-Y. Song, Z. Wang, M. Jantz, W. Schneider, M. Wu, E. Montoya, B. Kardasz, B. Heinrich, S. G. E. te Velthuis, H. Schultheiss, and A. Hoffmann, Damping in Yttrium Iron Garnet Nanoscale Films Capped by Platinum, Phys. Rev. Lett. **111**, 106601 (2013).

[11] J. Sinova, S. O. Valenzuela, J. Wunderlich, C. H. Back, and T. Jungwirth, Spin Hall effects, Rev. Mod. Phys. **87**, 1213 (2015).

[12] W. Zhang, W. Han, X. Jiang, S.-H. Yang, and S. S. P. Parkin, Role of transparency of platinum-ferromagnet interfaces in determining the intrinsic magnitude of the spin Hall effect, Nat. Phys. **11**, 496 (2015).

[13] K.-U. Demasius, T. Phung, W. Zhang, B. P. Hughes, S.-H. Yang, A. Kellock, W. Han, A. Pushp, and S. S. P. Parkin, Enhanced spin–orbit torques by oxygen incorporation in tungsten films, Nat. Commun. **7**, 10644 (2016).

[14] L. Liu, C.-F. Pai, Y. Li, H. W. Tseng, D. C. Ralph, and R. A. Buhrman, Spin-torque switching with the giant spin Hall effect of tantalum, Science **336**, 555 (2012).

[15] L. Liu, T. Moriyama, D. C. Ralph, and R. A. Buhrman, Spin-Torque Ferromagnetic Resonance Induced by the Spin Hall Effect, Phys. Rev. Lett. **106**, 036601 (2011).

[16] N. Nagaosa, J. Sinova, S. Onoda, A. H. MacDonald, and N. P. Ong, Anomalous Hall effect, Rev. Mod. Phys. **82**, 1539 (2010).

[17] S. Parkin and S.-H. Yang, Memory on the racetrack, Nat. Nano **10**, 195 (2015).

[18] S.-H. Yang, K.-S. Ryu, and S. Parkin, Domain-wall velocities of up to 750 m s-1 driven by exchange-coupling torque in synthetic antiferromagnets, Nat Nanotechnol. **10**, 221 (2015).

[19] K.-S. Ryu, L. Thomas, S.-H. Yang, and S. Parkin, Chiral spin torque at magnetic domain walls, Nat. Nanotechnol. **8**, 527 (2013).

[20] L. Thomas, Y. See-Hun, R. Kwang-Su, B. Hughes, C. Rettner, W. Ding-Shuo, T. Ching-Hsiang, S. Kuei-Hung, and S. S. P. Parkin, in *Electron Devices Meeting (IEDM), 2011 IEEE International* (IEEE, 2011), pp. 24.2.1.

[21] D. C. Ralph and M. D. Stiles, Spin transfer torques, J. Magn. Magn. Mater. **320**, 1190 (2008).

[22] L. Berger, Emission of spin waves by a magnetic multilayer traversed by a current, Phys. Rev. B **54**, 9353 (1996).

[23] J. C. Slonczewski, Current-driven excitation of magnetic multilayers, J. Magn. Magn. Mater. **159**, L1 (1996).

[24] I. I. Rabi, Space quantization in a gyrating magnetic field, Phys. Rev. **51**, 652 (1937).

[25] L. Allen and J. Eberly, *Optical Resonance and Two Level Atoms* (Dover Publications, New York, 1987).

[26] A. Capua, O. Karni, G. Eisenstein, V. Sichkovskyi, V. Ivanov, and J. P. Reithmaier, Coherent control in a semiconductor optical amplifier operating at room temperature, Nat. Commun. **5**, 5025 (2014).

[27] A. D. Karenowska, J. F. Gregg, V. S. Tiberkevich, A. N. Slavin, A. V. Chumak, A. A. Serga, and B. Hillebrands, Oscillatory Energy Exchange between Waves Coupled by a Dynamic Artificial Crystal, Phys. Rev. Lett. **108**, 015505 (2012).

[28] K. Yang, W. Paul, S.-H. Phark, P. Willke, Y. Bae, T. Choi, T. Esat, A. Ardavan, A. J. Heinrich, and C. P. Lutz, Coherent spin manipulation of individual atoms on a surface, Science **366**, 509 (2019).

[29] A. Capua, C. Rettner, S.-H. Yang, T. Phung, and S. S. P. Parkin, Ensemble-averaged Rabi oscillations in a ferromagnetic CoFeB film, Nat. Commun. **8**, 16004 (2017).

[30] M. Sargent, M. Scully, and W. Lamb, *Laser Physics* (CRC Press, FL, 1976).

[31] T. L. Gilbert, A phenomenological theory of damping in ferromagnetic materials, IEEE Trans. Magn. **40**, 3443 (2004).

[32] A. Capua, S.-H. Yang, T. Phung, and S. S. P. Parkin, Determination of intrinsic damping of perpendicularly magnetized ultrathin films from time-resolved precessional magnetization measurements, Phys. Rev. B **92**, 224402 (2015).

[33] J. E. Miltat and M. J. Donahue, in *Handbook of Magnetism and Advanced Magnetic Materials* (John Wiley & Sons, NJ, 2007).

[34] P. Krone, M. Albrecht, and T. Schrefl, Micromagnetic simulation of ferromagnetic resonance of perpendicular granular media: Influence of the intergranular exchange on the Landau–Lifshitz–Gilbert damping constant, J. Magn. Magn. Mater. **323**, 432 (2011).

[35] C. J. García-Cervera, Numerical Micromagnetics : A Review, Bol. Soc. Esp. Mat. Apl. **39**, 103 (2007).

[36] S. V. Vonsovskii, *Ferromagnetic Resonance* (Pergamon, Oxford, 1966).

[37] A. Capua, T. Wang, S.-H. Yang, C. Rettner, T. Phung, and S. S. P. Parkin, Phase-resolved detection of the spin Hall angle by optical ferromagnetic resonance in perpendicularly magnetized thin films, Phys. Rev. B **95**, 064401 (2017).